J. Fluid Mech. (1987), *vol.* 181, *pp.* 467–484
Printed in Great Britain

A reconsideration of the three-shock theory for a pseudo-steady Mach reflection

By G. BEN-DOR

Department of Mechanical Engineering, Ben-Gurion University of the Negev, Beer Sheva, P.O. Box 653, Israel

(Received 5 February 1986)

The analytical solution of a pseudo-steady Mach reflection was considered. It was found that the solution of the well-known perfect-gas conservation equations of a pseudo-steady Mach reflection – the three-shock theory – failed to accurately predict the angles between the incident, reflected and Mach stem shock waves. The disagreement between theory and experiments was not settled even when real-gas effects were accounted for. However, the inclusion of real-gas effects did improve the analytical predictions. In order to improve the analytical model, the boundary layers developing on both sides of the slipstream were integrated into the analysis. Using these boundary layers, the displacement thickness as a function of distance along the slipstream from the triple point was calculated. The displacement thickness was then related to the angular displacement of the slipstream, as a function of that distance. Finally it was shown that the displacement, taken at a distance equivalent to the incident-shock-wave thickness, could be used to obtain computed results which agree with experimentally measured data.

1. Introduction

When a planar shock wave encounters a sharp compressive corner, such as the leading edge of a wedge in a shock tube, two different types of reflection can occur. They are regular reflection and Mach reflection. The type of reflection that will occur depends for a given gas on the incident-shock-wave Mach number M and the reflecting wedge angle θ_{w}.

An unsteady Mach reflection, as obtained in shock-tube experiments over straight wedges, is shown schematically in figure 1. The Mach reflection consists of four discontinuities – the incident shock i, the reflected shock r, the Mach stem m and the slipstream s. These four discontinuities coincide at the triple point T. Over a plane wedge the triple point moves along a straight line making an angle χ with the wedge surface. The Mach stem is usually curved. In the case of weak shock waves it is concave while in the case of strong shock waves it is convex (Dewey & McMillin 1985*a*, *b*; Glass 1986).

The shock reflection process over plane wedges in shock tubes has been found by many experimentalists to be self-similar (Smith 1945; White 1951, 1952; Ben-Dor & Glass 1979; Dewey & McMillin 1985*a*, *b*). Their experimental investigations have clearly indicated that any point j on any of the shock waves in a given reflection, having a radius vector $\boldsymbol{r}$ with the tip of the wedge as origin, was transformed at a later time to a new point, $C\boldsymbol{r}$, where C is a scalar constant. This experimental observation means that instead of three independent variables x, y and t, the phenomenon is describable in terms of x/t and y/t, i.e. x and y may be measured

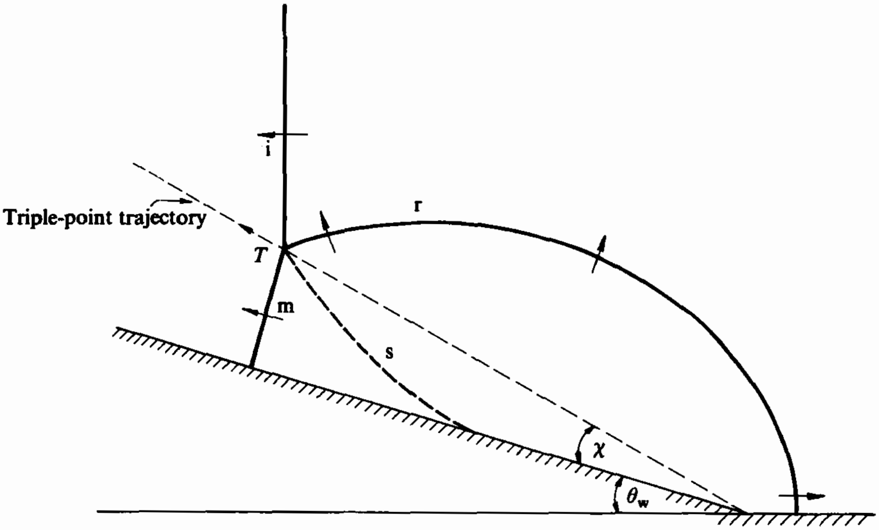

FIGURE 1. Schematic illustration of an unsteady Mach reflection. i, incident shock wave; r, reflected shock wave; m, Mach stem; s, slipstream; T, triple point; χ, triple point trajectory angle; θ_w, wedge angle.

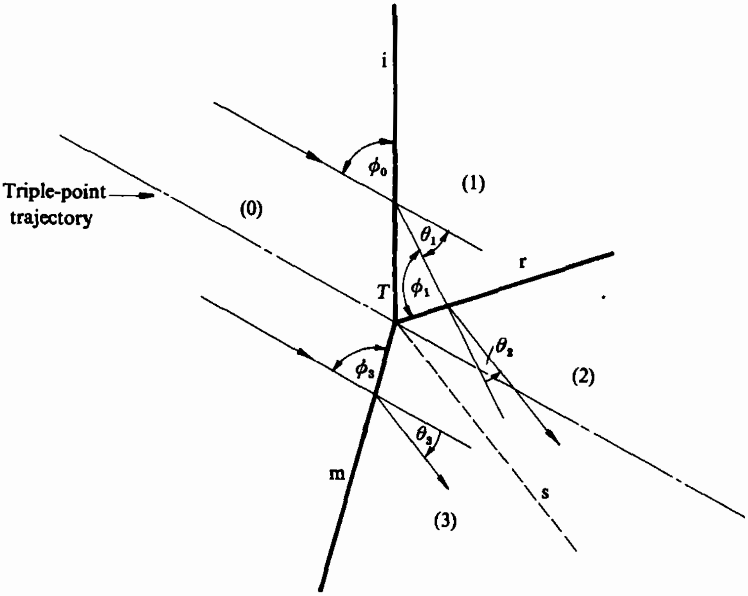

FIGURE 2. The wave configuration of a Mach reflection from a frame of reference attached to the triple point T: (0)–(3), thermodynamic states; ϕ, angle of incidence; θ, deflection angle; i, r, m and s are defined in the caption of figure 1.

relative to any point provided it moves with a constant velocity with respect to the leading edge of the wedge.

The triple point T has been traditionally chosen as such a point for analytical study of the Mach reflection phenomenon. By attaching a frame of reference to the triple point T, the unsteady Mach reflection shown in figure 1 is transformed to a pseudo-steady Mach reflection (figure 22). Unlike the reflection in the laboratory frame of reference (figure 1), the shock waves here are stationary. Thus, the incident i, reflected r and Mach stem m shocks can be treated using the steady flow theory. Assuming that at the vicinity of the triple point the shock waves are straight, the oblique-shock-wave conservation equations can be applied separately to the incident, reflected and Mach-stem shock waves. For each shock wave there are four conservation equations: conservation of mass, conservation of tangential momentum, conservation of normal momentum and conservation of energy. The conservation equation for i, r and m are (Ben-Dor 1978):

for i

$$\rho_0 u_0 \sin\phi_0 = \rho_1 u_1 \sin(\phi_0 - \theta_1), \tag{1}$$

$$\rho_0 \tan\phi_0 = \rho_1 \tan(\phi_0 - \theta_1), \tag{2}$$

$$p_0 + \rho_0 u_0^2 \sin^2\phi_0 = p_1 + \rho_1 u_1^2 \sin^2(\phi_0 - \theta_1), \tag{3}$$

$$h_0 + \tfrac{1}{2} u_0^2 \sin^2\phi_0 = h_1 + \tfrac{1}{2} u_1^2 \sin^2(\phi_0 - \theta_1); \tag{4}$$

for r

$$\rho_1 u_1 \sin\phi_1 = \rho_2 u_2 \sin(\phi_1 - \theta_2), \tag{5}$$

$$\rho_1 \tan\phi_1 = \rho_2 \tan(\phi_1 - \theta_2), \tag{6}$$

$$p_1 + \rho_1 u_1^2 \sin^2\phi_1 = p_2 + \rho_2 u_2^2 \sin^2(\phi_1 - \theta_2), \tag{7}$$

$$h_1 + \tfrac{1}{2} u_1^2 \sin^2\phi_1 = h_2 + \tfrac{1}{2} u_2^2 \sin^2(\phi_1 - \theta_2); \tag{8}$$

and for m

$$\rho_0 u_0 \sin\phi_3 = \rho_3 u_3 \sin(\phi_3 - \theta_3), \tag{9}$$

$$\rho_0 \tan\phi_3 = \rho_3 \tan(\phi_3 - \theta_3), \tag{10}$$

$$p_0 + p_0 u_0^2 \sin^2\phi_3 = p_3 + \rho_3 u_3^2 \sin^2(\phi_3 - \theta_3), \tag{11}$$

$$h_0 + \tfrac{1}{2} u_0^2 \sin^2\phi_3 = h_3 + \tfrac{1}{2} u_3^2 \sin^2(\phi_3 - \theta_3), \tag{12}$$

where ρ is the density, p the static pressure, h the enthalpy, u the flow velocity, ϕ the incident angle and θ the deflection angle. Subscripts 0, 1, 2 and 3 refer to the flow states as defined in figure 2. If thermodynamic equilibrium is assumed, then two thermodynamic properties are sufficient to define a state, e.g., $\rho = \rho(p, T)$, $h = h(p, T)$ etc. Thus, the above set of 12 equations consists of 18 variables, namely, p_0, p_1, p_2, p_3, T_0, T_1, T_2, T_3, u_0, u_1, u_2, u_3, ϕ_0, ϕ_1, ϕ_3, θ_1, θ_2 and θ_3. As will be shown subsequently, two additional equations arise from the fact that states (2) and (3) are separated by a contact surface. Thus, the entire set of 14 equations contains 18 variables. In order to make the set of the equations solvable, four of the above-listed variables must be known. Two of the four required variables arise from the initial conditions; they are the initial pressure p_0 and the initial temperature T_0. The additional two parameters that are usually determined prior to solving the set of equations at hand are u_0 and ϕ_0. These two parameters depend solely on the incident-shock-wave velocity u_i, the reflecting wedge angle θ_w and the triple-point trajectory angle χ, through the following expressions:

$$\phi_0 = 90^\circ - \theta_w - \chi,$$

$$u_0 = \frac{u_i}{\cos(\theta_w + \chi)}.$$

While u_i and θ_w are also known initial variables, χ must be either calculated using the analytical method presented by Ben-Dor (1981), or alternatively measured from an experimental photograph. Since the analytical approach does not agree with experiments in the entire range of incident-shock-wave Mach numbers and reflecting wedge angles, it was decided, for the sake of accuracy, to use the measured value of

χ from the photograph. Thus, with the measured value of χ and the initial values u_i and θ_w, the values of ϕ_0 and u_0 can be calculated from the above expressions, to lead to a closed set of 14 equations and 14 unknown variables.

As mentioned earlier, the two complementary equations needed to make the above set of equations solvable arise from the fact that the flow behind the reflected shock wave, state (2), is separated from the flow behind the Mach stem, state (3) (see figure 2), by a contact surface. Since the pressures on both sides of the contact surface must be equal, we have

$$p_2 = p_3. \tag{13}$$

Furthermore, if the contact region is assumed to be infinitely thin, i.e. a slipstream, then one obtains

$$\theta_3 = \theta_1 - \theta_2. \tag{14}$$

Thus, we now have a set of 14 equations with 14 unknowns which, in principle, is solvable.

In a recently conducted study the experimentally obtained angles between the various discontinuities were compared to those predicted analytically. The results of the comparison, as well as the recorded photographs, raised some serious doubts about the validity of the model described by (1)–(14), which is known as 'the three-shock theory'. The study is outlined in §2.

2. Present study

The experiment in question is shown in figure 3, which is a direct shadowgraph (also referred to as contact shadowgraph) of a pseudo-steady Mach reflection. Figure 4 is a blow-up of the Mach reflection shown in figure 3.

The experiment was conducted on the 4 cm × 8 cm shock tube of the Institute of High Speed Mechanics, Tohoku University, Sendai, Japan. The phenomenon was recorded using a giant pulse ruby laser. The initial conditions for the Mach reflection shown in figure 3 were: $M_i = 2.71 \pm 0.01$, $\theta_w = 47.1°$, $T_0 = 296$ K and $p_0 = 760$ Torr. The Mach-reflection structure is clearly seen in the photograph. The triple-point trajectory angle as measured from the photograph is $\chi = 3° \pm 0.5°$, and the angle between the incident shock wave i and the oncoming flow, in a frame of reference attached to the triple point, is measured to be $\phi_0 = 39.9° \pm 0.5°$, in total agreement with the relation $\phi_0 = 90° - (\theta_w + \chi)$.

Let us now define the following four angles: ω_{ir}, the angle between the incident and reflected shock waves; ω_{im}, the angle between the incident and Mach-stem shock waves; ω_{rs}, the angle between the reflected shock and the slipstream, and ω_{ms}, the angle between the Mach stem and the slipstream. These four angles can be related to the various incidence ϕ and deflection θ angles, which are defined in figure 2, in the following way:

$$\omega_{ir} = 180° + \theta_1 - \phi_0 - \phi_1, \tag{15}$$

$$\omega_{im} = 180° + \phi_0 - \phi_3, \tag{16}$$

$$\omega_{rs} = \phi_1 - \theta_2, \tag{17}$$

$$\omega_{ms} = \phi_3 - \theta_3. \tag{18}$$

Summing (15)–(18) results in

$$\omega_{ir} + \omega_{im} + \omega_{rs} + \omega_{ms} = 360° + \theta_1 - \theta_2 - \theta_3. \tag{19}$$

Inserting (14) into this relation results, as expected, in

$$\omega_{ir} + \omega_{im} + \omega_{rs} + \omega_{ms} = 360°.$$

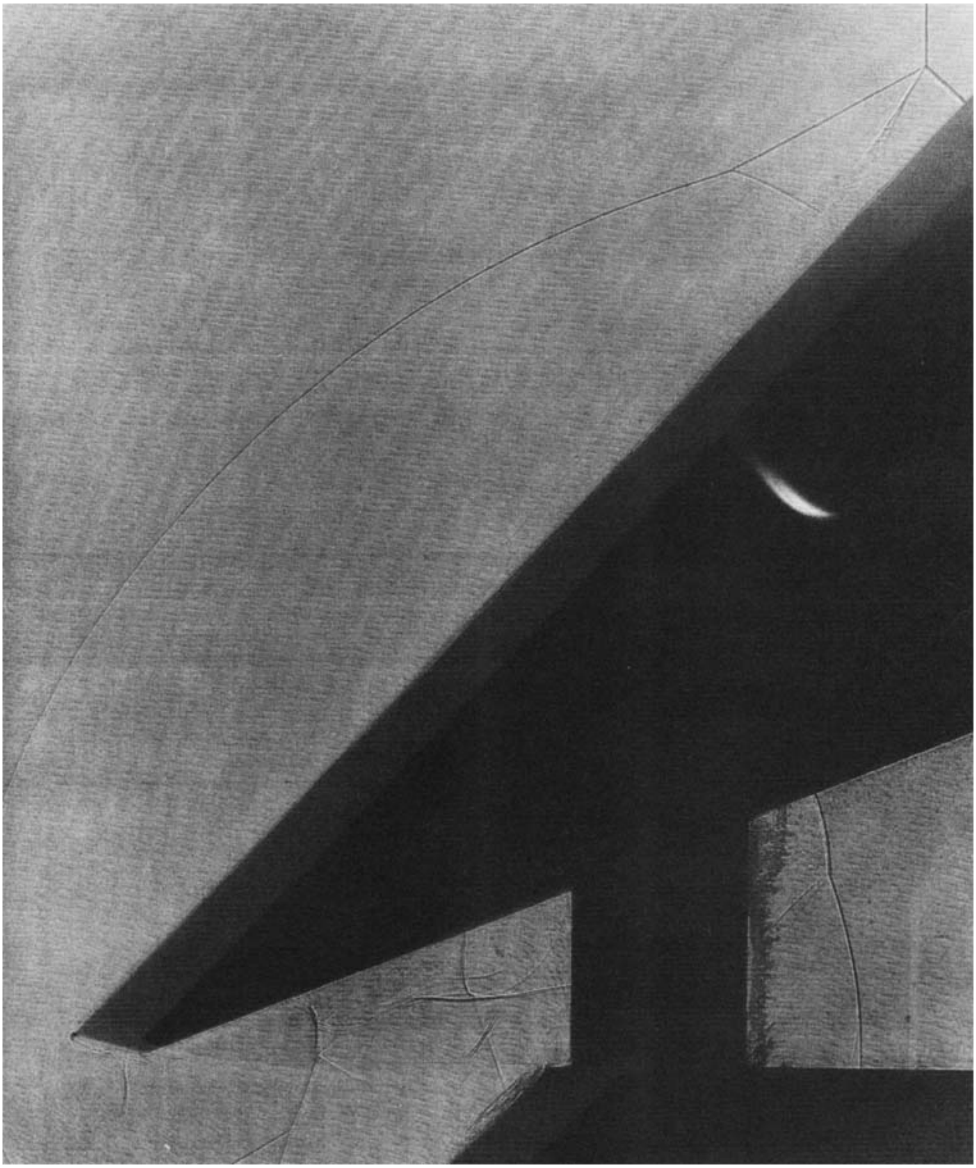

FIGURE 3. A shadowgraph of a Mach reflection in a shock tube: $M_i = 2.71$, $\theta_w = 47.1°$, $T_0 = 296$ K and $p_0 = 760$ Torr.

A computer program was written in order to solve (1)–(18) and obtain the flow properties and the angles between the various discontinuities in the vicinity of the triple point of a Mach reflection. For the initial conditions of the Mach reflection shown in figures 3 and 4, i.e. $M_i = 2.71$, $\phi_0 = 39.9°$, $T_0 = 296$ K and $p_0 = 760$ Torr, the perfect-gas solution results in

$$\omega_{im} = 132.8° \pm 0.7°, \quad \omega_{ir} = 123.0° \pm 1.12°, \quad \omega_{rs} = 27.27° \pm 0.58°.$$

The uncertainties of these computed angles result from those in the experimentally measured data used as input to the calculation, i.e. p_0, T_0, M_i and χ.

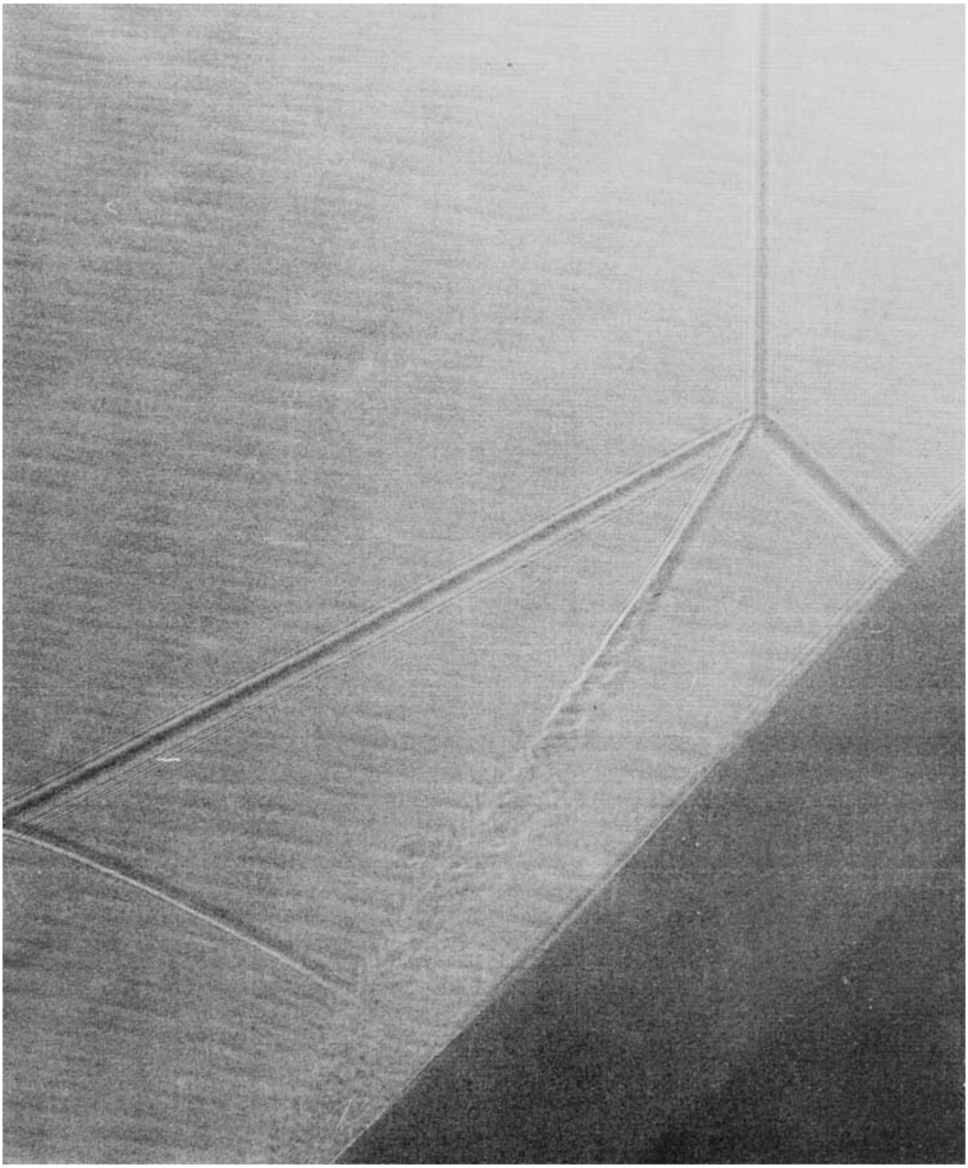

FIGURE 4. A blow-up of the vicinity of the triple point of the Mach reflection shown in figure 3.

The experimental values of these angles, as measured directly from figure 4, are

$$\omega_{\mathrm{im}} = 132^\circ \pm 1^\circ, \quad \omega_{\mathrm{ir}} = 118^\circ \pm 1^\circ, \quad \omega_{\mathrm{rs}} = 32^\circ \pm 1^\circ.$$

It can be clearly seen that the analytical prediction based on the three-shock theory fails to accurately predict the angles between the incident, the reflected and Mach-stem shock waves. While the analytical prediction of ω_{im} is about 0.8° greater than the corresponding measured value, and can therefore be considered as fairly good, the $\pm 5^\circ$ discrepancies between the predicted and measured values of ω_{ir} and ω_{rs} are far too large to be left unexplained.

In summary, the foregoing example clearly indicates that the inaccuracies involved in measuring the incident-shock-wave Mach number M_i and/or the incidence angle ϕ_0 cannot account for the disagreement between theory and experiment. (Note that since the model assumed perfect-gas behaviour, the inaccuracy in the measurements of the initial temperature T_0 and pressure p_0 did not play any role in the analytical predictions.)

The unexplained disagreement clearly suggests that something in the model described by (1)–(14) is wrong. In the following, two basic assumptions of the three-shock theory, (1)–(14), will be examined. The two assumptions are: (i) the gas behaves as a perfect gas; and (ii) the flow is inviscid.

Each of these assumptions is investigated separately by relaxing its constraints, i.e. by integrating into the three-shock theory real-gas effects for the first case and viscosity effects along the slipstream for the second, and then solving the governing equations.

3. The three-shock theory with real-gas effects

Ben-Dor & Glass (1979) showed that if real-gas effects are assumed to take place immediately behind the shock fronts, then the predictions of the real-gas model will start to differ from those of the perfect-gas model at $M_i > 2$, due to rotational–vibrational relaxation. At $M_i \approx 6$ the contribution of dissociational relaxation becomes significant and the solution starts to depend on the initial pressure p_0. Therefore, it can be concluded from the work of Ben-Dor & Glass (1979) that in the range $2 < M_i < 6$ the coupling between the rotational and vibrational degrees of freedom might play a significant role. It should be mentioned, however, that in reality, even when the internal degrees of freedom are excited, they do not reach their thermodynamic equilibrium immediately behind the shock front, but at a certain distance behind the shock front which terminates the relaxation zone. Inside the relaxation zone the flow is in a non-equilibrium state. Hence the above assumption, that the flow reaches a state of vibrational and rotational equilibrium immediately behind the shock front, is adopted for the sake of simplicity only, and therefore the results should be considered only as a first approximation.

Based on this discussion it was decided to assume that rotational and vibrational relaxation take place immediately behind the shock fronts. These relaxation mechanisms were added to the computer code. The computer program was then used to solve (1)–(14) for the following initial conditions: $M_i = 2.71 \pm 0.01$, $\theta_w = 47.1°$, $T_0 = 296 \pm 1$ K, $p_0 = 760 \pm 1$ Torr and $\chi = 3° \pm 0.5°$. The analytical results obtained are

$$\omega_{im} = 132.1° \pm 0.72°, \quad \omega_{ir} = 117.03° \pm 1.57°, \quad \omega_{rs} = 29.99° \pm 0.53°.$$

As shown earlier, the experimental results are

$$\omega_{im} = 132° \pm 1°, \quad \omega_{ir} = 118° \pm 1°, \quad \omega_{rs} = 32° \pm 1°.$$

It is obvious from these results that the inclusion of rotational and vibrational relaxation into the model has drastically improved the agreement between theory and the experiment as far as ω_{im}, ω_{ir} and ω_{rs} are concerned. However, ω_{rs} still differs by about 2° from the experimental result. The results clearly suggest that rotational and vibrational equilibrium must be accounted for if one is to analytically describe a Mach reflection, even at moderate incident-shock-wave Mach numbers (recall that at present $M_i = 2.71$). However, although the agreement between theory and the experiment has been tremendously improved when real-gas effects are accounted for, a yet unexplained disagreement still remains.

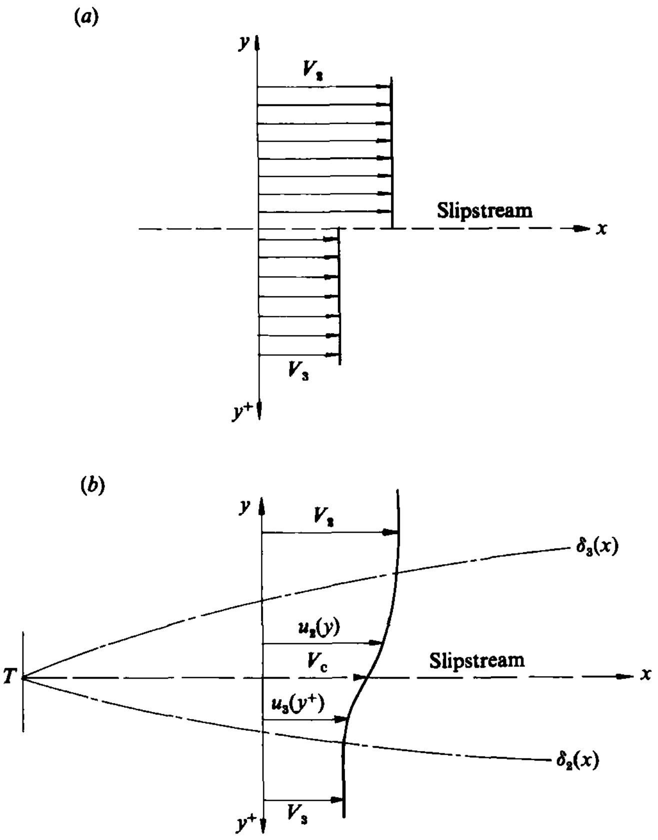

FIGURE 5. The flow velocity profiles on both sides of the slipstream; (a) inviscid flow; (b) real flow.

Note that for the real-gas model, small changes in the initial temperature T_0 and pressure p_0 were also investigated. Unfortunately, they also failed to explain the consistent gap between the analytical and experimental results. Thus, it is evident from the foregoing discussion that the experimental uncertainty in measuring the parameters M_1, ϕ_0, T_0 and p_0 cannot explain the failure of the three-shock theory to predict the experimental results, even when real-gas effects are accounted for.

4. The three-shock theory with viscous effects

As mentioned earlier, the solution of (1)–(14) assumes that the gas is inviscid. This implies that the flow velocity profiles on both sides of the slipstream are as shown in figure 5 (a), which indicates that the flow velocity is discontinuous at the slipstream. Above the slipstream the flow velocity is V_2, and below it V_3.

However, when two parallel streams of different velocities interact, boundary layers develop in both streams to yield a continuous change from V_2 to V_3. Lock (1950) has shown that these boundary layers could be treated 'using a method equivalent to that of Blasius for the boundary layer on a flat plate' (see the introduction to this paper). Furthermore, according to Lock (1950), Sir Geoffrey Taylor, in an unpublished note, has applied the von Kármán momentum-integral method to obtain a simple approximate solution. In the following, the von Kármán momentum method of analysing boundary layers will be adopted, in a way similar to that outlined by Lock (1950).

It should also be noted that the idea that the boundary layers that develop along the slipstream might modify the flow pattern sufficiently to account for the observed deviation was first introduced by Courant & Friedrichs (1948, p. 345). However, to the best of the author's knowledge this paper is the first quantitative attack on the problem. Momentum transfer between the flows on each side of the slipstream will produce a continuous flow velocity profile as shown in figure 5(*b*). Two boundary layers $\delta_2(x)$ and $\delta_3(x)$ start to grow at the triple point T $(x = 0)$, where x is a distance measured along the slipstream. Outside these boundary layers the flow velocities are V_2 and V_3 respectively. However, inside the boundary layers the flow velocity profiles change continuously. In the region above the slipstream the velocity profile inside the boundary layer is $u_2(y)$ and in the region below the slipstream it is $u_3(y^+)$. Each of these two profiles reaches a value of V_c on the slipstream.

Assuming that the flow inside the boundary layers is laminar, one can use the following general velocity profile for u_2:

$$u_2 = ay^3+by^2+cy+d. \tag{20}$$

With the following boundary conditions:

$$u(y=\delta_2) = V_2, \quad u(y=0) = V_c, \quad \frac{\partial u}{\partial y}(y=\delta_2) = 0, \quad \frac{\partial^2 u}{\partial y^2}(y=0) = 0,$$

one obtains

$$u_2 = \tfrac{1}{2}(V_c-V_2)\left(\frac{y}{\delta_2}\right)^3 - \tfrac{3}{2}(V_c-V_2)\left(\frac{y}{\delta_2}\right)+V_c. \tag{21}$$

The velocity profile u_3 can be obtained in a similar way, and is

$$u_3 = \tfrac{1}{2}(V_c-V_3)\left(\frac{y^+}{\delta_3}\right)^3 - \tfrac{3}{2}(V_c-V_3)\left(\frac{y^+}{\delta_3}\right)+V_c. \tag{22}$$

Defining $\eta_2 = V_c/V_2$ such that $0<\eta_2<1$ and $\eta_3 = V_c/V_3$ such that $\eta_3>1$ and inserting these definitions into (21) and (22) results in

$$u_2 = \tfrac{1}{2}V_2(\eta_2-1)\left(\frac{y}{\delta_2}\right)^3 - \tfrac{3}{2}V_2(\eta_2-1)\left(\frac{y}{\delta_2}\right)+\eta_2 V_2 \tag{23}$$

and

$$u_3 = \tfrac{1}{2}V_3(\eta_3-1)\left(\frac{y^+}{\delta_3}\right)^3 - \tfrac{3}{2}V_3(\eta_3-1)\left(\frac{y^+}{\delta_3}\right)+\eta_3 V_3. \tag{24}$$

Using the definitions following (22) one can write

$$\frac{\eta_2}{\eta_3} = \frac{V_3}{V_2}. \tag{25}$$

If one is to use the inviscid model (1)–(14), i.e. uniform flow profiles on both sides of the slipstream, then the slipstream must be displaced according to the displacement thickness. Among the various displacement thicknesses mentioned in the literature (Shames 1982, p. 362), the one based on conservation of mass has been used in the past few years quite successfully by Hornung & Taylor (1979) and Shirouzu & Glass (1982), who explained the persistence of regular reflection beyond its theoretical limit, and by Ben-Dor *et al.* (1987) who investigated the transition from regular to Mach reflection over rough surfaces. Therefore, in the following the mass displacement thickness will be adopted.

The mass boundary-layer-displacement thickness is defined as the distance by which the boundary (over which the fluid flows, i.e. the slipstream in the present case) would have to be displaced if the entire flow were imagined to be frictionless and the same mass flow maintained at any cross-section.

Thus, one can still use the inviscid model described by (1)–(14), but should account for an angular displacement of the slipstream.

As a first step, the boundary-layer thickness on each side of the slipstream must be developed. This is done in the following section.

5. The boundary-layer thickness

The boundary-layer thickness on each side of the slipstream can be obtained using the von Kármán momentum-integral technique (Shames 1982, p. 369). For the sake of simplicity it is assumed in the following that the flows on both sides of the slipstream are incompressible and that there is no pressure gradient along the slipstream. As will be shown subsequently, the distance along the slipstream that is relevant to the present analytical model is of the order of the shock-wave thickness; hence it is quite safe to assume that in such a short distance, the pressure and density changes are negligible. Under these assumptions, the von Kármán momentum integral assumes the following form (Shames 1982, p. 370):

$$-\frac{(\tau_w)_i}{\rho_i} = \frac{\partial}{\partial x}\int_0^{\delta_i} (u_i^2 - u_i V_i)\,\mathrm{d}y, \tag{26}$$

where subscript i can take the respective values 2 or 3 when representing the flows above or below the slipstream. The shear stress along the slipstream τ_w can be calculated from

$$(\tau_w)_i = \mu_i \left.\frac{\partial u_i}{\partial y_i}\right|_{y_i=0}. \tag{27}$$

Inserting the velocity profiles given by (23) and (24) into the above expressions finally results in the following expressions for the boundary-layer thickness on either side of the slipstream:

$$\frac{\delta_i}{x} = \left(\frac{280}{22\eta_i + 13}\right)^{\frac{1}{2}} (Re_{ix})^{-\frac{1}{2}}, \tag{28}$$

where
$$Re_{ix} = \frac{\rho_i V_i x}{\mu_i}.$$

Note that if η_i is set to be equal to zero, i.e. $u_i = 0$ at $y = 0$, (28) is reduced to the well-known relation for the boundary-layer thickness over a stationary flat plate (Shames 1982, p. 373),

$$\frac{\delta}{x} = 4.64 Re_x^{-\frac{1}{2}}.$$

6. The displacement thickness

Figures 6 (a, b) and 6 (c, d) illustrate the displacement of the slipstream for the flows in states (2) and (3) (see figure 2) respectively. As can be seen, the displacement thickness is positive for the fast flow V_2, while for the slower flow V_3 it is negative.

The displacement thickness in state (2) can be calculated (Shames 1982, p. 362) from

$$\int_0^{\delta_2} [V_2 - u_2(y)]\,\mathrm{d}y = V_2 \delta_2^*, \tag{29}$$

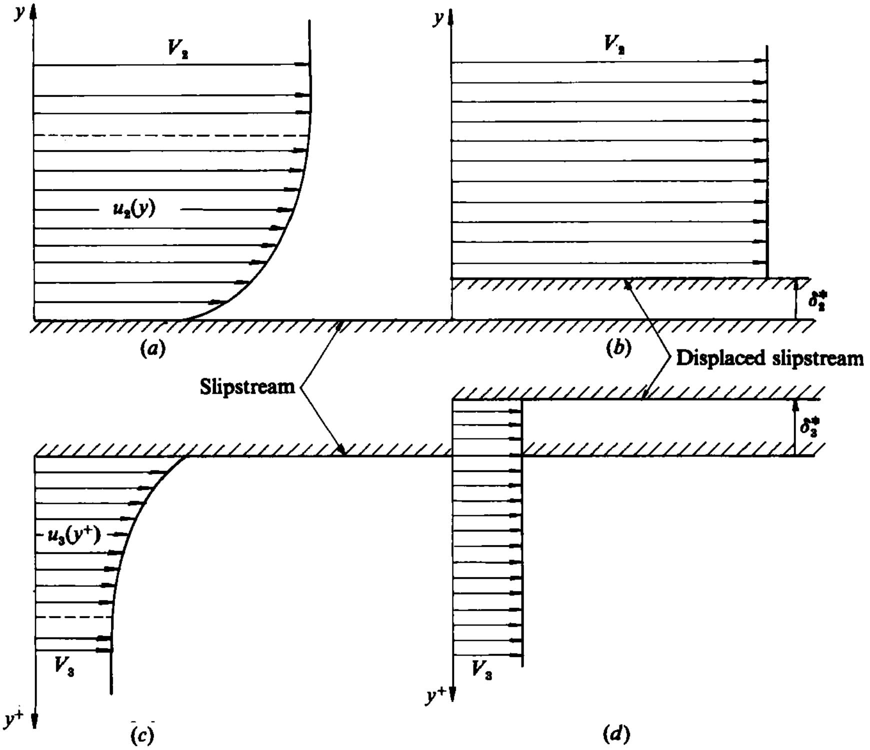

FIGURE 6. Schematic illustration of the displacement thickness: (*a*) the velocity profile of the viscous flow in state (2) over the slipstream; (*b*) uniform inviscid flow profile over the displaced slipstream in state (2) (note δ_2^* is positive); (*c*) the velocity profile of the viscous flow in state (3) over the slipstream; and (*d*) uniform inviscid flow profile over the displaced slipstream in state (3) (note δ_3^* is negative).

and in state (3) from

$$\int_0^{\delta_3} [u_3(y^+) - V_3]\,\mathrm{d}y^+ = V_3\,\delta_3^*. \tag{30}$$

Inserting (23) and (24) into (29) and (30) respectively results in

$$\delta_2^* = \tfrac{3}{8}(1-\eta_2)\,\delta_2, \quad \delta_3^* = \tfrac{3}{8}(\eta_3-1)\,\delta_3.$$

Inserting (28) with $i = 2$ and 3, respectively, into the above expressions results in

$$\frac{\delta_2^*}{x} = \tfrac{3}{8}(1-\eta_2)\left(\frac{280}{22\eta_2+13}\right)^{\frac{1}{2}}(Re_{2x})^{-\frac{1}{2}} \tag{31}$$

and

$$\frac{\delta_3^*}{x} = \tfrac{3}{8}(\eta_3-1)\left(\frac{280}{22\eta_3+13}\right)^{\frac{1}{2}}(Re_{3x})^{-\frac{1}{2}}, \tag{32}$$

but, at any given distance x, δ_2^* must be equal to δ_3^*; thus, from (31) and (32) one obtains

$$\frac{1-\eta_2}{\eta_3-1}\left(\frac{22\eta_3+13}{22\eta_2+13}\right)^{\frac{1}{2}} = \left[\frac{\mu_3}{\mu_2}\,\frac{\rho_2}{\rho_3}\,\frac{V_2}{V_3}\right]^{\frac{1}{2}}. \tag{33}$$

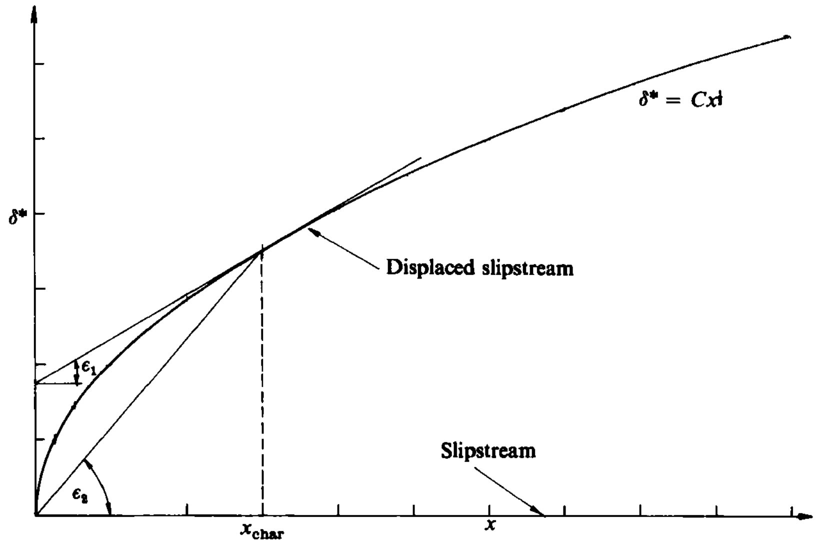

FIGURE 7. General dependence of the displacement thickness δ^* on x, and definition of two possible angular displacements of the slipstream.

Using the following expressions:

$$\frac{\mu}{\mu_0} = \left(\frac{T}{T_0}\right)^{\alpha}, \quad \rho = \frac{p}{RT},$$

and recalling that $p_2 = p_3$ (see (13)), results in

$$\frac{1-\eta_2}{\eta_3-1}\left(\frac{22\eta_3+13}{22\eta_2+13}\right)^{\frac{1}{2}} = \left[\left(\frac{T_3}{T_2}\right)^{1+\alpha}\frac{V_2}{V_3}\right]^{\frac{1}{2}}, \tag{34}$$

since

$$\frac{V_2}{V_3} = \frac{M_2}{M_3}\frac{a_2}{a_3} = \frac{M_2}{M_3}\left(\frac{T_2}{T_3}\right)^{\frac{1}{2}}, \tag{35}$$

where M, a and T are respectively the Mach number, the speed of sound and the temperature of the flow. Inserting (35) into (34) and (25) yields

$$\frac{1-\eta_2}{\eta_3-1}\left(\frac{22\eta_3+13}{22\eta_2+13}\right)^{\frac{1}{2}} = \left[\left(\frac{T_3}{T_2}\right)^{\frac{1}{2}+\alpha}\frac{M_2}{M_3}\right]^{\frac{1}{2}} \tag{36}$$

and

$$\frac{\eta_2}{\eta_3} = \frac{M_3}{M_2}\left(\frac{T_3}{T_2}\right)^{\frac{1}{2}}. \tag{37}$$

The above two equations provide a means for calculating η_2 and η_3, provided T_2, T_3, M_2 and M_3 are known. Note that according to Mazor, Ben-Dor & Igra (1985), $\alpha = 0.6487$ for a diatomic gas. For a monatomic gas $\alpha = 0.76$. Once η_2 and η_3 are known, the specific relations for δ_2^*/x or δ_3^*/x provide a means of determining the angular displacement of the slipstream.

Equations (31) and (32) indicate that even if the slipstream is straight, the displaced slipstream location δ^* is a function of $x^{\frac{1}{2}}$, as illustrated in figure 7, where the general dependence of δ^* upon x is shown. The slipstream that coincides with the x-axis is displaced, and assumes the shape of the curve $\delta^* = Cx^{\frac{1}{2}}$.

The angular displacement of the slipstream can be calculated using one of the following two expressions:

$$\epsilon = \tan^{-1}\left.\frac{d\delta^*}{dx}\right|_{x_{\mathrm{char}}} \tag{38}$$

or

$$\epsilon = \tan^{-1}\left.\frac{\delta^*}{x}\right|_{x_{\mathrm{char}}} \tag{39}$$

where x_{char} is a characteristic length.

The first expression, (38), gives the slope of the tangent of the δ^* curve at $x = x_{\mathrm{char}}$, i.e. ϵ_1 in figure 7, while (39) gives the average slope of the δ^* curve at $x = x_{\mathrm{char}}$, i.e. ϵ_2 in figure 7. Both of these possibilities were discussed quite extensively by Shirouzu & Glass (1982) and Ben-Dor *et al.* (1987), who concluded that (39) is the better one to be used. Ben-Dor *et al.* (1987) have further shown that $x_{\mathrm{char}} = l_s$, where l_s is the thickness of the incident or Mach stem shock waves. Hence, the characteristic length in the flow state behind the Mach stem, i.e. in state (3), is l_s. Since the flow in state (2) is obtained from state (0) by passing through both the incident and the reflected shocks, the characteristic length of state (2) might be longer. However, since both states (2) and (3) are adjacent to the slipstream, it is more appropriate to use the shorter lengthscale. The shock-wave thickness is about tenfold the mean free path λ, i.e. $l_s \approx 10\lambda$ (Glass 1986). Combining the above results in

$$x_{\mathrm{char}} \approx 10\lambda. \tag{40}$$

Thus the angular displacement of the slipstream is calculated from

$$\epsilon = \tan^{-1}\left.\frac{\delta^*}{x}\right|_{x=10\lambda}. \tag{41}$$

Once the angular displacement of the slipstream ϵ is known, the deflection of the flow through the reflected shock wave must be changed from θ_2 to $\theta_2+\epsilon$, while the deflection of the flow through the Mach stem must be changed from θ_3 to $\theta_3-\epsilon$, i.e. the flows must be parallel to the displaced slipstream. These two flow deflection angles result in two new angles of incident, ϕ_1^{d} and ϕ_3^{d} which change the predicted values of ω_{ir}, ω_{im} and ω_{rs} as calculated from (15), (16) and (17) respectively.

It should be mentioned here that the von Kármán momentum-integral technique was justified by comparing its results to those of Blasius (Shames 1982, p. 368). However, the results of Blasius arise from solving a simplified form of the Navier–Stokes equations (Shames 1982, §9.7). The simplified forms of the Navier–Stokes equations are known as the boundary-layer equations. Unfortunately, the simplified boundary-layer equations cannot be used in the vicinity of $x = 0$: the full Navier–Stokes equations should be solved there. However, because the foregoing approach was successful in explaining the von Neumann Paradox (Shirouzu & Glass 1982) and the transition from regular to Mach reflection over rough surfaces (Ben-Dor *et al.* 1987), it was adopted in this study too.

Therefore, one should recall that the present approach is a simplistic first-order approximation only.

7. Application of the new model to a Mach reflection

Equations (1)–(14) were solved for the following initial conditions: $M_1 = 2.71$, $\phi_0 = 39.9°$, $T_0 = 296$ K and $P_0 = 760$ Torr. The results obtained are shown in table 1.

State	M	p[Torr]	T[K]	ρ[gm/cm^3]	ϕ	θ
(0)	4.231	760	296	0.1154×10^{-2}	39.9°	—
(1)	2.171	6404	697.9	0.4124×10^{-2}	43.64°	26.73°
(2)	1.537	15707	920.6	0.7667×10^{-2}	—	16.49°
(3)	0.441	15707	1305.0	0.5409×10^{-2}	87.16°	10.24°

$\omega_{ir} = 123.19°$, $\omega_{im} = 132.74°$, $\omega_{rs} = 27.16°$

State	μ[gm/(cm s)]	a[cm/s]	V[cm/s]
(0)	1.801×10^{-4}	35070.0	148400.0
(1)	3.142×10^{-4}	53860.0	116900.0
(2)	3.7846×10^{-4}	61860.5	95079.6
(3)	4.7463×10^{-4}	73651.8	32480.5

TABLE 1. Predictions from the analytical solution of (1)–(14) for the following initial conditions: $M_0 = 4.231$, $\phi_0 = 39.9°$, $T_0 = 296$ K and $p_0 = 760$ Torr, perfect-gas model

Inserting T_2, T_3, M_2 and M_3 into (36) and (37) results in $\eta_2 = 0.4527$ and $\eta_3 = 1.3251$. Inserting these values into (28), (31) and (32) leads to

$$\frac{\delta_2}{x} = 3.492(Re_{2x})^{-\frac{1}{2}}, \tag{42}$$

$$\frac{\delta_2^*}{x} = 0.7167(Re_{2x})^{-\frac{1}{2}}, \tag{43}$$

$$\frac{\delta_3}{x} = 2.577(Re_{3x})^{-\frac{1}{2}}, \tag{44}$$

$$\frac{\delta_3^*}{x} = 0.3142(Re_{3x})^{-\frac{1}{2}}. \tag{45}$$

Inserting (43) into (41) yields

$$\epsilon = \tan^{-1}\left[0.7167\left(\frac{\mu_2}{\rho_2 V_2 x_{\text{char}}}\right)^{\frac{1}{2}}\right].$$

From Glass (1986), the mean free path at sea level is about 6.6×10^{-6} cm; therefore according to (40), $x_{\text{char}} = 6.6\times10^{-5}$ cm. Inserting this value, together with those given in table 1 for μ_2, ρ_2 and V_2, gives

$$\epsilon = 3.63°.$$

Therefore, the new flow deflection through the reflected shock wave calculated from $\theta_2+\epsilon$ is $16.49°+3.63° = 20.12°$ and the new flow deflection through the Mach-stem shock wave calculated from $\theta_3-\epsilon$ is $10.24°-3.63° = 6.61°$ (θ_2 and θ_3 are taken from table 1).

For the flow Mach number ahead of the reflected shock wave, i.e. $M_1 = 2.171$, the value of the angle of incidence required to deflect the flow by 20.12° is $\phi_1^d = 48.81°$. For the flow Mach number ahead of the Mach stem shock wave, i.e. $M = 4.231$, the value of the angle of incidence required to deflect the flow by 6.61° is $\phi_3^d = 88.20°$. Inserting these new values of ϕ_1^d and ϕ_3^d into (15)–(17) gives

$$\omega_{ir} = 118.02°, \quad \omega_{im} = 131.70°, \quad \omega_{rs} = 32.32°.$$

State	M	p[Torr]	T[K]	ρ[gm/cm^3]	ϕ	θ
(0)	4.231	760.0	296.0	0.1154×10^{-2}	39.9°	—
(1)	2.458	4454.9	566.0	0.3537×10^{-2}	47.42°	24.64°
(2)	1.698	11086.4	741.7	0.6717×10^{-2}	—	17.61°
(3)	0.553	11086.4	968.1	0.5146×10^{-2}	87.95°	7.04°

$$\omega_{\mathrm{ir}} = 117.32^\circ,\quad \omega_{\mathrm{im}} = 131.95^\circ,\quad \omega_{\mathrm{rs}} = 29.81^\circ$$

State	μ[gm/(cm s)]	a[cm/s]	V[cm/s]
(0)	1.801×10^{-4}	35070.0	148400.0
(1)	2.742×10^{-4}	47990.0	116900.0
(2)	3.290×10^{-4}	54180.0	91990.0
(3)	3.910×10^{-4}	60910.0	33670.0

TABLE 2. Predictions of the analytical solution of (1)–(14) for the following initial conditions: $M_0 = 4.231$, $\phi_0 = 39.9$, $T_0 = 296$ K and $p_0 = 760$ Torr, real-gas model

Comparing these values with those measured in the photograph, i.e.

$$\omega_{\mathrm{ir}} = 118^\circ\pm1^\circ,\quad \omega_{\mathrm{im}} = 132^\circ\pm1^\circ,\quad \omega_{\mathrm{rs}} = 32^\circ\pm1^\circ,$$

indicates that the analytical predictions are in excellent agreement with the experimental results.

8. The three-shock theory with viscosity and real-gas effects

It was shown earlier that the inclusion of real-gas effects into the three-shock theory tremendously improved the analytical prediction. Consequently, it is of interest to check the proposed model when real-gas effects are integrated into it.

The results of the solution of (1)–(14) with real-gas effects are shown in table 2. Inserting T_2, T_3, M_2 and M_3 into (36) and (37) results in $\eta_2 = 0.4946$ and $\eta_3 = 1.3292$. These results are quite similar to those obtained when the gas is assumed to be perfect, i.e. $\eta_2 = 0.4527$ and $\eta_3 = 1.3251$. Inserting the real-gas values of η_2 and η_3 into (28), (31) and (32) yields

$$\frac{\delta_2}{x} = 3.424(Re_{2x})^{-\frac{1}{2}}, \tag{46}$$

$$\frac{\delta_2^*}{x} = 0.6490(Re_{2x})^{-\frac{1}{2}}, \tag{47}$$

$$\frac{\delta_3}{x} = 2.575(Re_{3x})^{-\frac{1}{2}}, \tag{48}$$

$$\frac{\delta_3^*}{x} = 0.3178(Re_{3x})^{-\frac{1}{2}}. \tag{49}$$

Inserting (47) into (41) results in

$$\epsilon = \tan^{-1}\left[0.6490\left(\frac{\mu_2}{\rho_2 V_2 x_{\mathrm{char}}}\right)^{\frac{1}{2}}\right]$$

which, for the data shown in table 2 and $x_{\mathrm{char}} = 6.6\times10^{-5}$ cm, yields

$$\epsilon = 3.34^\circ.$$

Therefore, the new flow deflection through the reflected shock wave $(\theta_2+\epsilon)$ is 20.95° and the new flow deflection through the Mach-stem shock wave $(\theta_3-\epsilon)$ is 3.70° (θ_2 and θ_3 are taken from table 2).

For the flow Mach number ahead of the reflected shock wave, i.e. $M_1 = 2.458$, the value of the angle of incidence required to deflect the flow by 20.95° is $\phi_1^{\mathrm{d}} = 44.7°$. For the flow Mach number ahead of the Mach-stem shock wave, i.e. $M_0 = 4.231$, the value of the angle of incidence required to deflect the flow by 3.7° is $\phi_3^{\mathrm{d}} = 89°$. Inserting these new values of ϕ_1^{d} and ϕ_3^{d} into (15)–(17) results in

$$\omega_{\mathrm{ir}} = 120.04°, \quad \omega_{\mathrm{im}} = 130.70°, \quad \omega_{\mathrm{rs}} = 27.09°.$$

These results indicate that the inclusion of real-gas effects into the boundary-layer analysis results in worse agreement than the perfect-gas boundary-layer analysis. However, since both the perfect-gas and the real-gas boundary-layer models involve simplifying assumptions it is impossible to state whether real-gas effects should or should not be accounted for.

9. Transition of the boundary layers from laminar to turbulent flow

The transition of the boundary layer from laminar to turbulent flow occurs when the Reynolds number Re_x reaches the critical value $Re_{x_{\mathrm{cr}}} = 3.2\times10^5\text{–}10^6$ (Shames 1982, p. 380), i.e.

$$x_{\mathrm{cr}} = (3.2\times10^5\text{–}10^6)\frac{\mu}{\rho V}.$$

Using the flow properties listed in table 1 for states (2) and (3) results in

$$(x_{\mathrm{cr}})_2 = (0.166\text{–}0.519)\ \mathrm{cm}, \quad (x_{\mathrm{cr}})_3 = (0.864\text{–}2.7)\ \mathrm{cm}.$$

If one assumes that the transition of the flow from laminar to turbulent inside the boundary layer occurs at the point where the slipstream starts to diverge rapidly and show the turbulent structure, then this point, as measured from the photograph shown in figures 3 and 4 is located 0.332 cm behind the triple point. This value falls well into the region predicted by $(x_{\mathrm{cr}})_2$. Note, that once the flow inside the boundary layer in state (2) changes from laminar to turbulent it influences the flow inside the boundary layer in state (3) and forces it to transition from laminar to turbulent at values of $Re_{x_{\mathrm{cr}}}$ smaller than those quoted above. (For further details see Shames 1982, p. 379.)

10. Discussion and conclusions

Table 3 summarizes the values obtained for ω_{ir}, ω_{im} and ω_{rs} using the various models presented in this paper. The numbers in brackets are the differences between the calculated and measured values.

It is clear from table 3 that the three-shock-theory prediction is inaccurate when the gas is assumed to be inviscid and perfect. However, when real-gas effects are accounted for, and the gas is still assumed to be inviscid, but in rotational–vibrational equilibrium immediately behind the shock fronts, the predictions of the three-shock theory are tremendously improved.

The best agreement with the experimental results is obtained when viscosity effects along the slipstream are integrated into the three-shock theory and a perfect-gas behaviour is assumed. For this case all the predicted values are well within the range of the experimental accuracy.

Type of model	ω_{ir}	ω_{im}	ω_{rs}
Experimental results	118° ± 1°	132° ± 1°	32° ± 1°
Three-shock theory for a perfect gas	123.19° (+5.19°)	132.74° (+0.74°)	27.16° (−4.84°)
Three-shock theory for a real gas in rotational–vibrational equilibrium	117.32° (−0.68°)	131.95° (−0.05°)	29.81° (−2.19°)
Three-shock theory for a perfect gas with viscous effects along the slipstream	118.02° (+0.02°)	131.70° (−0.30°)	32.32° (+0.32°)
Three-shock theory for a real gas in rotational–vibrational equilibrium with viscous effects along the slipstream	120.04° (+2.04°)	130.70° (−1.30°)	27.09° (−4.91°)

TABLE 3. Comparison between the results of the various models for $M_i = 2.71$, $\phi_0 = 39.9°$, $T_0 = 296$ K, $p_0 = 760$ Torr

Inclusion of real-gas effects into the three-shock theory together with viscosity effects results in a deterioration of the comparison between theory and experiment. The reason could be that the present real-gas model assumes rotational–vibrational equilibrium immediately behind the shock fronts, while the flow is known to have a relaxation zone before it reaches its equilibrium stage.

The present study clearly indicates that if one wishes to accurately predict the angles between the various shock waves of a pseudo-steady Mach reflection, one should account for viscosity effects along the slipstream, as well as real-gas effects.

Viscosity effects are included by calculating the boundary layers on both sides of the slipstream as a function of the distance along the slipstream from the triple point, and using the displacement-thickness technique to obtain the angular displacement of the slipstream. This angular displacement results in a new orientation of the various shock waves and the slipstream. However, as mentioned earlier the proposed model should be considered as a first approximation only, for the full set of the Navier–Stokes equations should be solved in order to obtain an exact solution. Hopefully, the proposed model will prove useful to others who may take up the idea and develop a more accurate one.

Finally it should be mentioned that Henderson (1964) showed that (1)–(14) can be reduced to a simple polynomial of order 10, with the pressure ratio p_3/p_0 as the polynomial variable. The polynomial coefficients were taken to be functions of the specific-heat-capacity ratio γ, the flow Mach number in state (0) M_0, and the pressure ratio across the incident shock wave p_1/p_0. Although a polynomial of degree ten yields ten mathematical roots, Henderson (1964) showed that, from simple physical considerations and the possibility of double roots, seven out of the ten roots can be discarded. This implies that the three-shock theory for a perfect inviscid gas does not yield a unique solution. This feature has not been removed by either of the two proposed modifications of the three-shock theory.

I would like to thank Professor H. Hornung for his suggestion to use the boundary-layer-displacement-thickness technique in order to resolve the disagreement between theory and experiments. I am also thankful to Professor K. Takayama for supplying me with the experimental records.

REFERENCES

BEN-DOR, G. 1978 *UTIAS Rep.* 232.

BEN-DOR, G. 1981 *AIAA J.* **19**, 531.

BEN-DOR, G. & GLASS, I. I. 1979 *J. Fluid Mech.* **92**, 459.

BEN-DOR, G., MAZOR, G., TAKAYAMA, K. & IGRA, O. 1987 *J. Fluid Mech.* **176**, 333.

COURANT, R. & FRIEDRICHS, K. O. 1948 *Supersonic Flow and Shock Waves.* Interscience.

DEWEY, J. M. & MCMILLIN, D. J. 1985*a* *J. Fluid Mech.* **152**, 49.

DEWEY, J. M. & MCMILLIN, D. J. 1985*b* *J. Fluid Mech.* **152**, 67.

GLASS, I. I. 1986 *AIAA Paper* 86-0306.

HENDERSON, L. F. 1964 *Aero. Q.* **XV**, 181.

HORNUNG, H. G. & TAYLOR, J. R. 1979 *J. Fluid Mech.* **90**, 541.

LOCK, R. C. 1950 *Q. J. Mech. Appl. Maths* **4**, 42.

MAZOR, G., BEN-DOR, G. & IGRA, O. 1985 *AIAA J.* **23**, 636.

SHAMES, I. H. 1982 *Mechanics of Fluids.* McGraw-Hill.

SHIROUZU, M. & GLASS, I. I. 1982 *UTIAS Rep.* 264.

SMITH, L. G. 1945 *OSRD Rep.* 6271.

WHITE, D. R. 1951 *Dept. Phys., Princeton Univ. Tech. Rep.* II-10.

WHITE, D. R. 1952 *Proc. 2nd Midwestern Conference on Fluid Mechanics.*